

# Ferrofluids and magnetically guided superparamagnetic particles in flows: A review of simulations and modeling

Shahriar Afkhami · Yuriko Renardy

Received: date / Accepted: date

**Abstract** Ferrofluids are typically suspensions of magnetite nanoparticles, and behave as a homogeneous continuum. The production of nanoparticles with a narrow size distribution and the achievement of colloidal stability are important technological issues. The ability of the ferrofluid to respond to an external magnetic field in a controllable manner has made it emerge as a smart material in a variety of applications, such as seals, lubricants, electronics cooling, shock absorbers and adaptive optics. Magnetic nanoparticle suspensions have also gained attraction recently in a range of biomedical applications, such as cell separation, hyperthermia, MRI, drug targeting and cancer diagnosis. In this review, we provide an introduction to mathematical modeling of three problems: motion of superparamagnetic nanoparticles in magnetic drug targeting, the motion of a ferrofluid drop consisting of chemically bound nanoparticles without a carrier fluid, and the breakage of a thin film of a ferrofluid.

**Keywords** Ferrofluid, Superparamagnetic nanoparticles, Volume-of-Fluid method, Thin film approximation

## 1 Introduction

This review presents three aspects of the mathematical analysis of the motion of superparamagnetic particles and drops in a surrounding fluid, under the influence of an external magnetic field: drug targeting, ferrofluid drop deformation, and instabilities and dewetting of a thin ferrofluid film. These problems are important

---

This work is partially supported by NSF-DMS-1311707 and NSF-CBET-1604351.

---

Shahriar Afkhami  
Department of Mathematical Sciences, New Jersey Institute of Technology, Newark, NJ 07102  
USA  
E-mail: shahriar.afkhami@njit.edu

Yuriko Renardy  
Department of Mathematics, Virginia Polytechnic and State University, Blacksburg, VA 24061  
USA  
E-mail: renardy@vt.edu

for a number of biomedical applications. The motion of a magnetic particle is determined by a force balance of the magnetic force, drag, and stochastic forces. The motion of a ferrofluid drop is affected by its deformation. Simulations using the Volume-of-Fluid method are presented. Once a drop reaches the target and coats it, a thin film approximation yields insight into instabilities and breakup. We refer the reader to recent publications, which in turn contain more comprehensive references and historical reviews.

An advantage of magnetic drug targeting is the delivery of drugs to specific tissues via the blood vessels as pathways under externally applied magnetic fields. Progress towards robust biomedical applications relies on the synthesis of appropriately coated nanoparticles, clusters and ferrofluids [1, 2, 3, 4]. Pros and cons of directing the magnetic nanoparticles in blood vessels and tissues are described in [5, 6, 7, 8, 9, 10]. Recent reviews highlight the use of magnetic nanoparticles in many biomedical applications; for instance, drug targeting, magnetic fluid hyperthermia, design of devices to measure targeting efficiency, and tissue engineering [11, 12, 13, 14, 15, 16].

In [17], the mathematical modeling of the transport of paramagnetic particles in viscous flow is described in terms of dipole points in an external magnetic field, with particle interactions for larger particles and higher concentrations [18]. Numerical approaches using Brownian dynamics for particle interactions in aggregation and disaggregation are being developed [19]. Technological applications include the sorting of not only cells but proteins and other biological components by biochemically functionalized paramagnetic beads that are manufactured to be attracted to specific targets. The mixture flows in a fluid, and as they move through a channel, magnetic fields deflect the desired cells to migrate toward predetermined exits. In [20], paramagnetic beads floating in a liquid are subjected to a magnetic field normal to the flow. The deflection by the magnetic field steers the beads towards a target whose location depends on the field and on the properties of the bead. An application to removing pathogens from the blood stream is shown in [21], reproduced in figure 1. Here the magnetic particles bind to pathogens such as bacteria. In addition to the motion of the particles, a model for the kinetics of this binding mechanism is formulated.

The design of the superparamagnetic nanoparticles involves uniformity in the small size. Of particular interest is the formation of a ferrofluid from chemically bonding many of them. Unlike the colloidal suspension of magnetite particles, this ferrofluid avoids the migration of the particles in the suspending fluid at high fields. This advantage is seen in the works of [22, 23, 24] for the potential treatment of retinal detachment by magnetically guiding a ferrofluid drop to seal the site. In particular, figure 2(a) shows a sample transmission electron microscopy (TEM) image of the magnetite nanoparticles at 300000 times magnification, and (b) shows the narrow size distribution. These particles are relevant to section 2. The magnetic nanoparticles are coated with biocompatible polydimethylsiloxane (PDMS) oligomers, and bonded to manufacture a ferrofluid. Figures 2(c-d) show experimentally observed states for the ferrofluid drop suspended in glycerol in uniform magnetic fields. The modeling in section 3.2 concerns the numerical simulation of stable equilibrium configurations under applied uniform magnetic fields. A series of experiments conducted under low and high magnetic field strengths are presented in [2] to understand the behavior of PDMS ferrofluid drops in uniform magnetic fields. Figure 3 shows the experiments in [2] of the drop at equilibrium

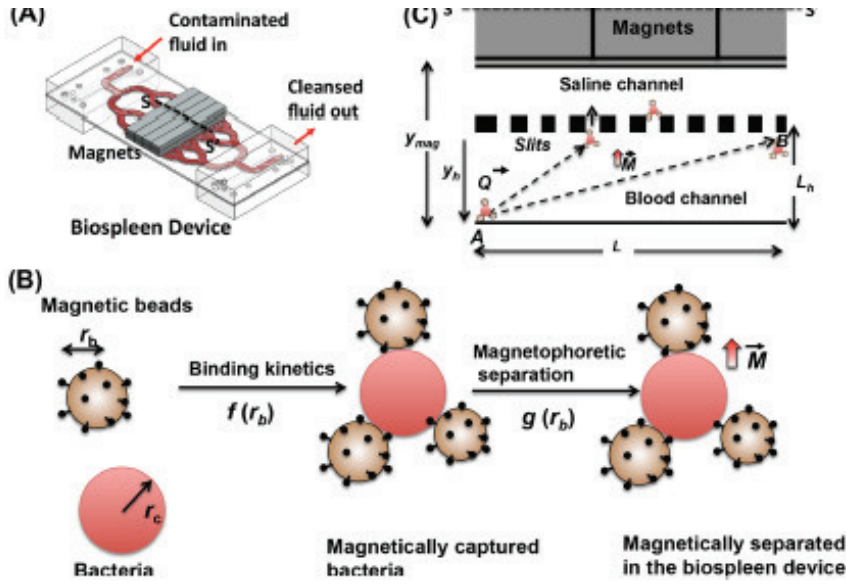


**Fig. 1** With permission from [21]. Summary of caption: ‘(A) A schematic design of the biospleen that magnetically cleanses fluids contaminated with bacteria using magnetic nanoparticles coated with FcMBL. (B) The magnetic separation process dissociated into two sequential phases; magnetic beads binding to cells and magnetic separation of cell - magnetic bead complexes. (C) A cross-sectional view of the biospleen channel through which magnetic bead-bound bacteria flow while they are deflected upward by external magnets on the top. If bacteria that passed position A reach the other side of the channel before they pass position B, we can assume that they are completely removed.’

for the magnetic field strengths varying from  $6.032$  to  $162.33 \text{ kA m}^{-1}$ . These results are revisited in section 3.2. For an updated review of literature on ferrofluid drop deformation in uniform magnetic fields, see [25].

The numerical investigation of the motion of a ferrofluid drop may be complicated by the highly distorted material interface. An advantage of the boundary integral method for three-dimensional (3D) drop deformation in Stokes flow is that the three-dimensionality is turned into a two-dimensional surface computation; this together with a high order surface discretization has been able to track viscous drops with high curvature, up to the first pinch-off [27,28]. However, this method does not extend easily to non-Newtonian models such as a power-law model that is suggested for blood flow. Novel nonsingular boundary integral methods are improving the accuracy and numerical stability of the 3D drop deformation in viscous flow at low inertia, including the influence of a magnetic field for constant magnetic susceptibility [29]. The effect of rotating magnetic field is investigated with the boundary integral formulation in [30]. The study of rotating magnetic fields on ferrofluid drops is of importance in many fields including astrophysics, and we refer the reader to recent reviews [31,32]. A limitation of the boundary integral formulation is that it is no longer applicable if the magnetic behavior is nonlinear.

Numerical algorithms with a diffuse-interface method have been developed for a droplet or layer in a uniform and rotating magnetic fields [32]. Intricate equilibrium shapes arise in the Rosensweig instability which originally refers to a ferrofluid

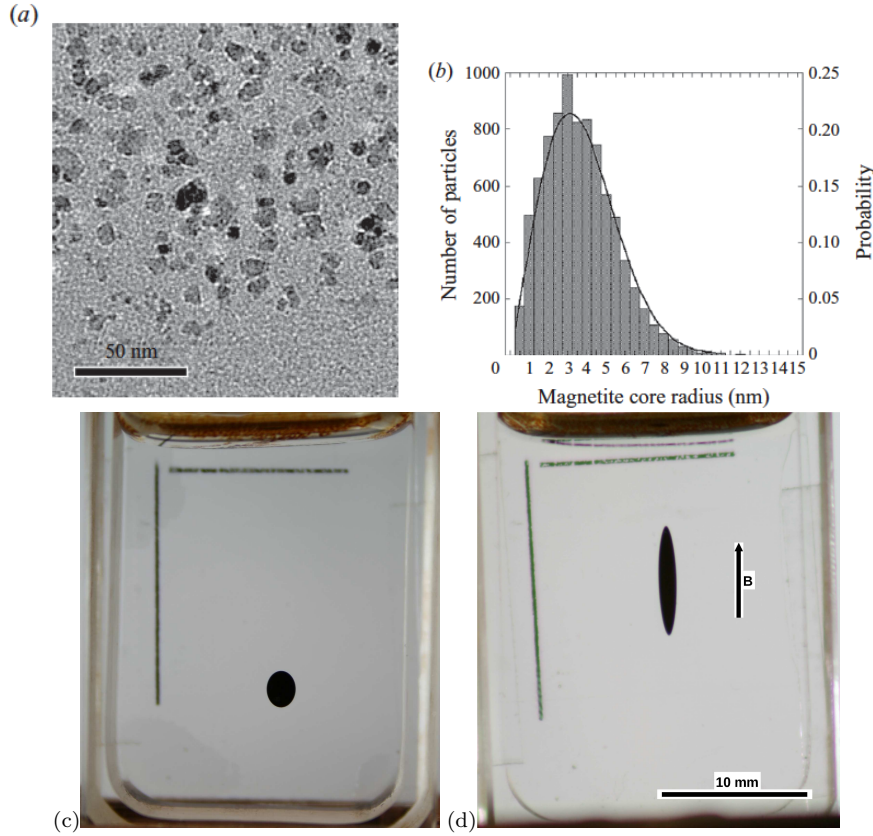


**Fig. 2** (a) Representative TEM image of PDMS-magnetite particles. (b) Histogram of the radii of the magnetite cores. From [22] and [23]. Experimental photographs of the deformation of a PDMS ferrofluid drop in a viscous medium under applied uniform magnetic fields of  $6.38 \text{ kA m}^{-1}$  (c) and  $638.21 \text{ kA m}^{-1}$  (d). From [26] with permission.

layer under magnetic force, surface tension force, gravity and hydrodynamics [33, 34, 35, 36]. In [37], the Rosensweig instability is investigated numerically for the diffusion of magnetic particles. The magnetic particle concentration and the free surface shape are part of the solution. A finite element method is used for Maxwell's equations and a finite difference method is used for a parametric representation of the free surface. A finite element formulation is developed and used in [38] to simulate the interaction of two or more particles in uniform and rotating magnetic fields. The interaction is significant in dense suspensions or larger sizes. In section 3.2, we focus on a Volume-of-Fluid formulation of [26] which is capable of utilizing a non-constant susceptibility, time-dependent evolution, and interface breakup and reconnection.

Finally, thin films driven by a magnetic field have been studied recently [39, 40]. These models are derived for the flow of a thin ferrofluid film on a substrate in the same spirit as the previous work by Craster and Matar [41] for the case of a leaky dielectric model. The derivation for a nonconducting ferrofluid simplifies

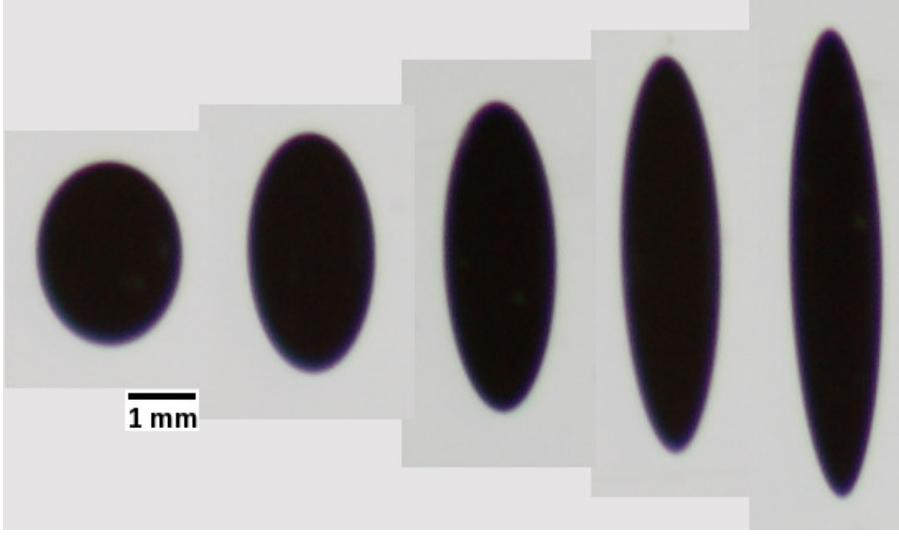


**Fig. 3** Photographic images from [26] of the drop equilibrium shape taken at magnetic field strengths 6.032, 12.167, 23.947, 59.762, 162.33  $\text{kA m}^{-1}$  (from left to right).

since there is no interfacial charge involved. The work of Seric et al. [39] includes the van der Waals force to impose the contact angle using the disjoining/conjoining pressure model and studies the film break up and the formation of satellite (secondary) droplets on the substrate under an external magnetic field. In section 3.5, we focus on a thin film approximation of ferrofluid on a substrate subjected to an applied uniform magnetic field and present the results of the magnetic field induced dewetting of thin ferrofluid films and the consequent appearance of satellite droplets.

## 2 Mathematical modeling of magnetic drug targeting

In this section, we summarize the set-up and results of [42]. One of the simplest model problems for predicting the accuracy of drug targeting concerns superparamagnetic nanoparticles of at most several nanometers diameter, and flowing through a venule of order  $10^{-4}$  m radius; see figures 4 (a - b). The velocity is  $(u(y, z, t), 0, 0)$  where  $u$  denotes the axial component. The no-slip conditions at the walls  $y^2 + z^2 = R^2$  and the Stokes equation are applied. For such a small radius, the effect of cardiac pumping on pressure fluctuations is negligible; therefore,  $u = u_{max}(1 - \frac{r^2}{R^2})$ , where the flow rate  $\frac{\pi}{2}u_{max}R^2$  is typically  $10^{-10}\text{m}^3\text{s}^{-1}$  [44]. This gives  $u_{max} \approx 0.006\text{m s}^{-1}$ . This flow generates a Stokes drag force on a solid sphere:  $\mathbf{F}_v = -(6\pi\eta a)(\frac{d\mathbf{x}}{dt} - (u, 0, 0))$  where  $\eta$  is the viscosity,  $a$  the radius,  $\mathbf{x}$  is the location of the particle, and  $D$  is the friction coefficient. For a larger blood vessel, the oscillatory component of the flow can be estimated from the systolic and diastolic blood pressure data.

The external magnetic field  $\mathbf{H}_e$  without a particle is known from experimental measurements and is used to calculate the field in the presence of the particle.

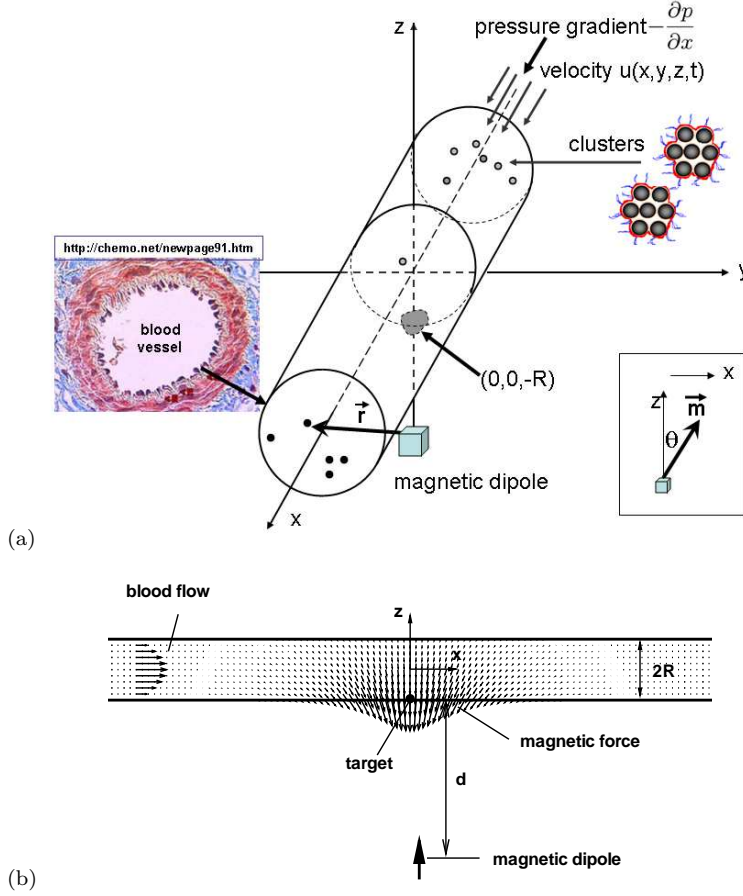


**Fig. 4** (a) (Figure 1 of [42]) The target is at  $(0, 0, -R)$ , in a cylindrical blood vessel of radius  $R$ . A magnetic point dipole is defined by the dipole moment vector  $\mathbf{m}$ , directed from the magnet placed below the target, and at an angle  $\theta$  to the positive  $x$ -axis; i.e.,  $\theta = 0$  is upward. The cross-sectional slide is from [43]. (b) (Figure 6 of [42]) Schematic of the vertical slice through the cylindrical vessel at  $y = 0$ . The magnetic force field is shown when the dipole is at a distance  $d$  below the vessel wall.

Under the assumptions of constant susceptibility  $\chi$  (magnetic field not too high), the permeability is  $\mu = \mu_0(1 + \chi)$ , where  $\mu_0$  denotes the permeability of vacuum. Maxwell's equations ( $\text{curl } \mathbf{H}_e = \mathbf{0}$ ,  $\text{div } \mathbf{H}_e = 0$ ) give  $\mathbf{H}_e = \nabla\phi$ , where  $\phi$  is a harmonic function. The external magnet is modeled by a magnetic dipole. We find the actual field  $\mathbf{H}$  with the particle by using the known formula  $\phi = \frac{-1}{4\pi} \frac{\mathbf{m} \cdot \mathbf{r}}{r^3}$ , where the vector  $\mathbf{r}$  points from the dipole to the particle. Provided that the external magnet is small, it is approximately a point dipole. This magnetic field exerts a force on the particle:  $\mathbf{F}_m = \int \mu_0(\mathbf{M} \cdot \nabla) \mathbf{H}_e dV$  where  $\mathbf{M} = \chi \mathbf{H}$  denotes the magnetization corresponding to the magnetic field  $\mathbf{H}$  with a particle of volume  $V = \frac{4}{3}\pi a^3$ , namely the Clausius-Mossotti formula [34, 45]  $\mathbf{M} = \frac{3\chi}{3+\chi} \mathbf{H}_e$ . This is used to calculate  $\mathbf{F}_m$ . The governing equation must satisfy  $\mathbf{F}_m + \mathbf{F}_v = \mathbf{0}$ . This is a system of nonlinear ordinary differential equations.

The superparamagnetic particles and clusters addressed in [42] are small enough that the Néel relaxation time and the magnetization are instantaneous compared with the motion to be solved[3]. However, we need to keep in mind that Brownian motion should be included if thermal energy  $kT$  becomes comparable to magnetic energy  $\mu_0 MHV$ , where  $k$  denotes Boltzmann's constant,  $T$  is in degrees Kelvin,  $H$  is the field and  $V$  is the volume of the particle. This estimate gives the diameter to be smaller than  $(6kT/\pi\mu_0 MH)^{1/3}$  ((2.2) of [34]). In the examples below, this is diameter of order  $10^{-8}$  m. We incorporate Langevin's model for Brownian motion through a stochastic forcing vector. This leads to the system

$$\rho V \frac{d^2 \mathbf{x}}{dt^2} = -D \left( \frac{d\mathbf{x}}{dt} - \mathbf{u}_b \right) + \frac{3\chi V \mu_0}{3 + \chi} \nabla \left( \frac{1}{2} |\nabla \phi|^2 \right) + \frac{\sqrt{2DkT}}{\sqrt{dt}} \mathbf{N}(0, 1), \quad (1)$$

where  $\rho$  is the density of the particle/cluster, and  $\mathbf{u}_b$  is the base flow. The left hand side term denotes acceleration which is estimated to be relatively small.  $N_1(0, 1)$ ,  $N_2(0, 1)$  and  $N_3(0, 1)$  denote independently generated, normally distributed, random variables with zero mean and unit variance. The random variables  $N_i(0, 1)$ ,  $i = 1, 2, 3$ , are constants over very short time intervals  $dt$ , and change randomly with a Gaussian distribution. Finally, the stochastic ordinary differential equation for the state vector  $X(t) = \mathbf{x}^T = (x(t), y(t), z(t))^T$  is,

$$dX = f(X)dt + g dW, \quad (2)$$

$$f(X) = \left[ \mathbf{u}_b(\mathbf{x}, t) + \frac{3\chi V \mu_0}{(3 + \chi)D} \nabla \left( \frac{1}{2} |\nabla \phi(\mathbf{x})|^2 \right) \right]^T, \quad (3)$$

$$g = \sqrt{\frac{2kT}{D}} \mathbf{I}; \quad (4)$$

$\mathbf{I}$  is the  $3 \times 3$  identity matrix,  $f(X(t))$  is the  $3 \times 1$  drift-rate vector,  $g$  is a  $3 \times 3$  instantaneous diffusion-rate matrix, and  $dW(t)$  denotes the vector  $\sqrt{dt} \mathbf{N}(0, 1)$ .

## 2.1 Numerical algorithm

The system (4) is integrated using the Euler-Maruyama method. At the  $n$ th time step, where  $\Delta t$  denotes a fixed step size,  $X_{n+1} = X_n + \Delta t f(X_n) + g(X_n) \Delta W_n$ . As detailed in [46], the advantage of this method is the strong convergence under broad assumptions. We use the implementation in the SDE Toolbox for Matlab [47]. The capture rate for a particle is defined to be the probability of hitting the tumor, which is situated at  $|x| < R_{tumor}$  at the wall in figure 4. Figure 5(a) shows sample trajectories, initially at  $x = -R_{tumor}$ , where  $R_{tumor}$  denotes the radius of the tumor at the wall. A trajectory can escape without hitting the wall (—), or escape after hitting the wall (—), or be captured at the target. Figures 5(b-d) use data from [26, 44]. The magnet is  $d = 0.03$  m outside the vessel wall; vessel radius  $R = 10^{-4}$  m,  $u_{max} = \frac{2}{\pi} 0.01 \text{ ms}^{-1}$ , particle radius  $a = 10^{-7}$  m,  $\eta = 0.004 \text{ Pa s}$ ,  $R_{tumor} = 100R$ , constant susceptibility  $\chi = 0.2$ . (b) shows the capture rate versus dipole moment  $m$ . For larger  $m$ , a non-constant Langevin fit approximates the magnetization data [26]. The capture rate scales with the square of the dipole moment even when the velocity profile is slightly blunted at the centerline which may relate to blood flow. To optimize the capture rate, it is

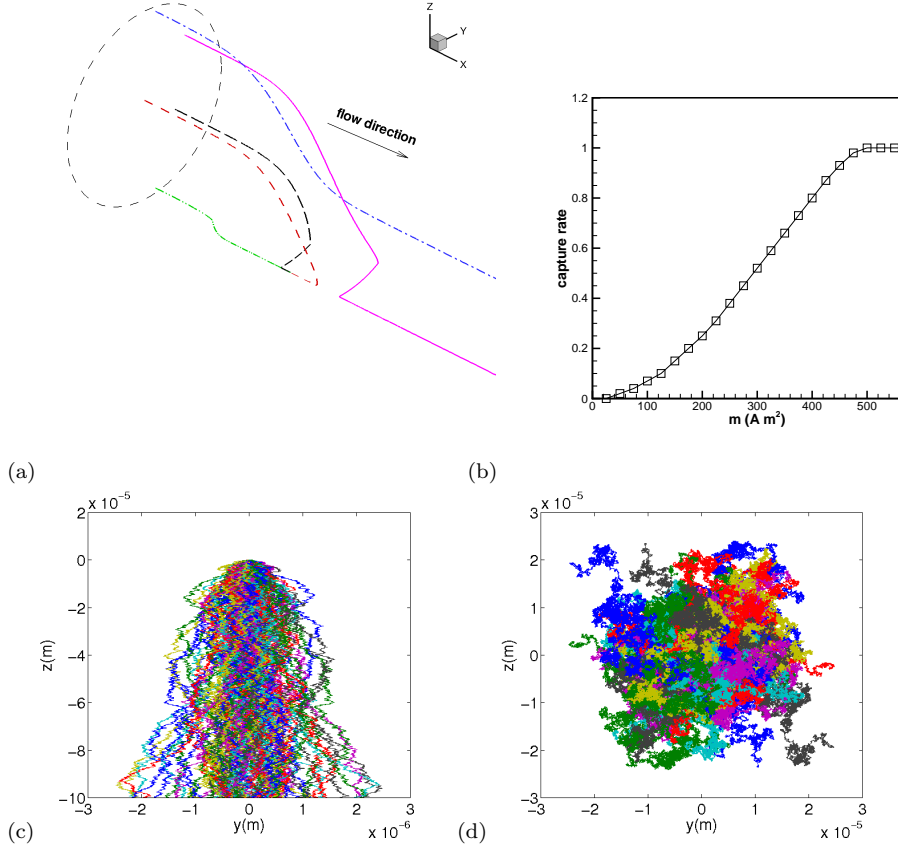


**Fig. 5** Reproduced with permission from [42]. (a) Typical trajectories with sliding motion on the wall. The scale is compressed in the  $x$ -direction.  $R = 10^{-4}$  m,  $u_{max} = \frac{2}{\pi} \times 10^{-2}$  m s $^{-1}$ ,  $a = 10^{-7}$  m,  $\eta = 0.004$  Pa s,  $\chi = 0.2$ ,  $m = 1$  A m $^2$ , and  $d = 50R$ . The clusters are released from  $x = -100R$ , the target is at  $x = 0$ . (b) Capture rate *vs.* dipole moment  $m$  with  $d = 0.03$  m,  $\chi = 0.2$ . (c) Trajectories in the  $y$ – $z$  plane with  $x = 0$  (target).  $m = 1056$  A m $^2$ ,  $\chi = 0.2$ ,  $\Delta t = 2 \times 10^{-4}$  s. 100 trajectories. (d) With smaller particles,  $a = 10^{-8}$  m.

found that the distance  $d$  should match the tumor size. (c) shows trajectories for  $a = 10^{-7}$  m, and compared with this, (d) shows that Brownian motion makes a significant difference for  $a = O(10^{-8})$  m.

The capture rate is optimal for a magnet that produces a strong field and a focused effect, and therefore high field gradients. This is one of the technological challenges in magnetic drug targeting. Recent studies show that arrays of magnets, such as the Halbach array, are an improvement over the single magnet. The balance of magnetic force and hydrodynamic drag for Stokes flow is calculated for high field gradient arrays and compared with experimental data in [48]. This gives guidance on how the particle trajectories depend on magnet shapes and arrays.



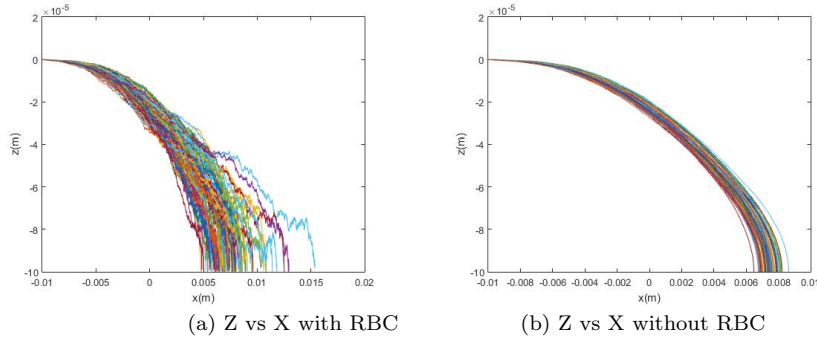


**Fig. 6** (with permission from [51], Figures 5(a-b)) 100 particle trajectories with point dipole magnetic field model and Cherry viscosity model with  $\mathbf{m} = [0, 0, 700Am^2]$ . Without red blood cell collisions, the capture rate was 100%. With red blood cell collisions, the capture rate was 91%.

Non-Newtonian effects in blood flow have been studied with empirical formulas that replace the Stokes drag coefficient [49]. For example, in the case of the larger arterial speeds, an empirical viscosity term which incorporates shear-thinning at the local shear rate is applied to write approximate equations for the motion of micron sized magnetic particles in Poiseuille flow [50,51]. The particles in [50] are of micron size, much larger than the nanometers considered in [42], and also the diameter of the artery and flow speeds are much larger, and therefore the Brownian effect for the particles is small. The use of the local shear rate of the background flow in the Stokes drag formula is an ad-hoc substitution. For a particle moving in non-Newtonian flow, such as in a shear-thinning fluid, the calculation of drag is tractable for quiescent flow, not for non-quiescent flow such as shear flow. Unlike Stokes flow, the equations are nonlinear so that solutions can not be superposed. The real velocity of the particle is spatially and temporally varying in response to the magnetic field and flow. A separate effect is the influence of red blood cells on the capture rate. [51] applies a formula for shear-enhanced diffusion in colloidal suspensions (equation (1) of [52]) to estimate that the red blood cells contribute an additive term proportional to the shear rate inside the square root in equation 4. Particle trajectories for the Cherry viscosity model and including the diffusion due to interaction with red blood cells are investigated in [51]. They find that the additional diffusion deteriorates the capture rate; figure 6 shows this.

### 3 Mathematical modeling of ferrofluid drops

To investigate the response of a ferrofluid droplet to an applied magnetic field, extra effort is needed to solve the details of the magnetic field, which in turn requires the knowledge of the shape of the interface. The non-local moving boundary problem which couples the spatial variation of the magnetic field with the interfacial shape of the drop necessitates a direct numerical computation. Numerical algorithms that explicitly track the interface and use finite element methods are developed to investigate equilibrium shapes of ferrofluid drops and interfacial instabilities in [53,54,55,56,57]. For the case of constant magnetic susceptibility,

a boundary-integral formulation is used to study equilibrium shapes for high-frequency rotating magnetic fields [30]. Numerical algorithms that implicitly track the interface include the Volume-of-Fluid (VOF) methods, Level-Set methods and diffuse-interface (DI) methods [58, 59, 60]. Each of these methods can be applied to subcases of the results we show below. We specifically describe the VOF method because of its simplicity, efficiency and robustness for tracking topologically complex evolving interfaces. However, this as well as other approaches has its limitations. An advantage is that it conserves mass and with the recent improvements in the discretization of the surface tension force, it remains a competitive method for modeling interfacial flows. We present these results in section 3.2.

A recent study has shown that a ferrofluid droplet on a hydrophobic substrate breaks up into two daughter droplets and a smaller satellite droplet under a sufficiently strong magnetic field [61]. These experiments also show that if the magnetic field is increased even further, the droplets break up again and rearrange to form an assembly of droplets on the substrate. In the same spirit, we present a model derived in [39] for the flow of a thin ferrofluid film on a substrate. The results in [39] show the film break up and the deformation of sessile droplets on the substrate under an external magnetic field. We present this study in section 3.5

### 3.1 Governing equations

The equations governing the motion of an incompressible ferrofluid drop suspended in another fluid are the conservation of mass and the balance of momentum

$$\frac{\partial \rho}{\partial t} + \mathbf{u} \cdot \nabla \rho = 0, \quad (5)$$

$$\rho \frac{\partial \mathbf{u}}{\partial t} + \mathbf{u} \cdot \nabla \mathbf{u} = -\nabla p + \nabla \cdot (2\eta \mathbf{D}) + \nabla \cdot \mathbf{\Pi}_M + \rho \mathbf{g}, \quad (6)$$

where  $\mathbf{u}(\mathbf{x}, t)$  is the velocity field,  $p(\mathbf{x}, t)$  the pressure,  $\rho(\mathbf{x}, t)$  and  $\eta(\mathbf{x}, t)$  are the phase dependent density and viscosity, respectively,  $\mathbf{D} = \frac{1}{2}(\nabla \mathbf{u} + (\nabla \mathbf{u})^T)$  is the rate of deformation tensor (where  $T$  denotes the transpose),  $\rho \mathbf{g} = -\rho g \hat{z}$  the body force due to gravity and  $\hat{z}$  the unit vector in the  $z$ -direction (with gravitational constant  $g$ ), and  $\mathbf{\Pi}_M(\mathbf{x}, t)$  is the magnetic stress tensor

$$\mathbf{\Pi}_M = -\frac{\mu_0}{2}(\mathbf{H} \cdot \mathbf{H})\mathbf{I} + \mu \mathbf{H}\mathbf{H}, \quad (7)$$

where  $\mathbf{I}$  is the identity tensor. The Maxwell equations for the magnetic induction  $\mathbf{B}$ , magnetic field  $\mathbf{H}$ , and magnetization  $\mathbf{M}$  are the magnetostatic Maxwell equations for a non-conducting ferrofluid

$$\nabla \cdot \mathbf{B} = 0, \quad \nabla \times \mathbf{H} = 0, \quad (8)$$

$$\mathbf{B}(\mathbf{x}, t) = \begin{cases} \mu_d \mathbf{H} & \text{in ferrofluid drop} \\ \mu_m \mathbf{H} & \text{outside ferrofluid drop,} \end{cases} \quad (9)$$

where  $\mu_d$  denotes the permeability of the drop, and  $\mu_m$  is the permeability of the surrounding fluid. Here, we assume that the surrounding fluid has a permeability very close to that for a vacuum,  $\mu_0$ . Therefore, we shall set  $\mu_m = \mu_0$  throughout. A magnetic scalar potential  $\psi$  is defined by  $\mathbf{H} = \nabla \psi$ , and satisfies

$$\nabla \cdot (\mu \nabla \psi) = 0. \quad (10)$$

For linear magnetic materials, the magnetization is a linear function of the magnetic field given by  $\mathbf{M} = \chi \mathbf{H}$ , where  $\chi = (\mu/\mu_0 - 1)$  is the magnetic susceptibility. The magnetic induction  $\mathbf{B}$  is therefore  $\mathbf{B} = \mu_0(\mathbf{H} + \mathbf{M}) = \mu_0(1 + \chi)\mathbf{H}$ . To describe the paramagnetic susceptibility quantitatively, the Langevin function  $L(\alpha) = \coth \alpha - \alpha^{-1}$  is used to describe the magnetization versus the magnetic field as

$$\mathbf{M}(\mathbf{H}) = M_s L\left(\frac{\mu_0 m |\mathbf{H}|}{k_B T}\right) \frac{\mathbf{H}}{|\mathbf{H}|}, \quad (11)$$

where the saturation magnetization,  $M_s$ , and the magnetic moment of the particle,  $m$ , enter as parameters,  $T$  denotes the temperature, and  $k_B$  is the Boltzmann's constant.

Let  $[\![\cdot]\!]$  denote the difference,  $\cdot_{\text{surrounding}} - \cdot_{\text{drop}}$ , at the interface between the ferrofluid drop and the external liquid. Let  $\mathbf{n}$  denote the unit normal outwards from the interface, and  $\mathbf{t}_1$  and  $\mathbf{t}_2$  denote the orthonormal tangent vectors. We require

1. The continuity of velocity, the normal component of magnetic induction, the tangential component of the magnetic field, the tangential component of surface stress,

$$[\![\mathbf{u}]\!] = \mathbf{0}, \quad \mathbf{n} \cdot [\![\mathbf{B}]\!] = 0, \quad \mathbf{n} \times [\![\mathbf{H}]\!] = \mathbf{0}, \quad [\![\mathbf{t}_1^T \cdot \boldsymbol{\Sigma} \cdot \mathbf{n}]\!] = 0, \quad [\![\mathbf{t}_2^T \cdot \boldsymbol{\Sigma} \cdot \mathbf{n}]\!] = 0.$$

2. The jump in the normal component of stress balanced by capillary effects,

$$[\![\mathbf{n}^T \cdot \boldsymbol{\Sigma} \cdot \mathbf{n}]\!] = \sigma k,$$

where  $\boldsymbol{\Sigma} = p - \rho g z + (2\eta \mathbf{D}) + \boldsymbol{\Pi}_M$ ,  $k = -\nabla \cdot \mathbf{n}$  is the interface curvatures, and  $\sigma$  is the interfacial tension.

### 3.2 One-fluid formulation and Volume-of-Fluid method

We take advantage of the axial symmetry present in the motion and deformation of a ferrofluid droplet placed in a viscous medium under an externally applied magnetic field and resort to the formulation in axisymmetric cylindrical coordinates  $(r, z)$ . The VOF method represents each liquid with a color function as

$$C(r, z, t) = \begin{cases} 0 & \text{in the surrounding medium} \\ 1 & \text{in the ferrofluid drop,} \end{cases} \quad (12)$$

which is advected by the flow. The position of the interface is reconstructed from  $C(r, z, t)$ . The one-fluid formulation of the governing equations (6) and (5) then reads

$$\frac{\partial C}{\partial t} + \mathbf{u} \cdot \nabla C = 0, \quad (13)$$

$$\rho \frac{\partial \mathbf{u}}{\partial t} + \mathbf{u} \cdot \nabla \mathbf{u} = -\nabla p + \nabla \cdot (2\eta \mathbf{D}) + \nabla \cdot \boldsymbol{\Pi}_M + \mathbf{F}_s + \rho \mathbf{g}, \quad (14)$$

where  $\mathbf{F}_s$  denotes the continuum body force due to interfacial tension [62]

$$\mathbf{F}_s = \sigma k \delta_s \mathbf{n}, \quad (15)$$

$\mathbf{n} = \nabla C/|\nabla C|$ ,  $\delta_s = |\nabla C|$  is the delta-function at the interface,  $\rho = \rho(C)$ ,  $\eta = \eta(C)$ , and  $\mu = \mu(C)$ . The magnetic potential  $\psi$  in axisymmetric cylindrical coordinates satisfies equation (10),

$$\frac{1}{r} \frac{\partial}{\partial r} \left( \mu r \frac{\partial \psi}{\partial r} \right) + \frac{\partial}{\partial z} \left( \mu \frac{\partial \psi}{\partial z} \right) = 0. \quad (16)$$

The dimensionless variables, denoted by tildes, are defined as follows

$$\begin{aligned} \tilde{\mathbf{x}} &= \frac{\mathbf{x}}{L_c} & \tilde{t} &= \frac{t}{\tau} \\ \tilde{\mathbf{u}} &= \frac{\tau}{L_c} \mathbf{u} & \tilde{\mathbf{g}} &= \frac{\mathbf{g}}{g} \\ \tilde{\mathbf{F}}_s &= \frac{\mathbf{F}_s}{\sigma/L_c^2} & \tilde{\mathbf{\Pi}}_M &= \frac{\mathbf{\Pi}_M}{H_o} \\ \tilde{p} &= \frac{p}{\sigma/L_c} & \tilde{\rho} &= \frac{\rho}{\rho_d}, \quad \tilde{\eta} = \frac{\eta}{\eta_d}, \quad \tilde{\mu} = \frac{\mu}{\mu_0} \end{aligned}$$

where  $L_c$ ,  $\tau$ ,  $H_o$  and  $g$  are characteristic scales of length, time, magnetic field and gravitational acceleration, respectively. The ferrofluid density and viscosity are  $\rho_d$  and  $\eta_d$ , respectively. For the choice of viscous time scale,

$$\tau = \frac{\eta_d L_c}{\sigma},$$

corresponding to the viscous length scale

$$L_c = \frac{\eta_d^2}{\rho_d \sigma},$$

equation (14) becomes, dropping the tilde notation,

$$\text{Oh}^{-2} \left( \rho \frac{\partial \mathbf{u}}{\partial t} + \mathbf{u} \cdot \nabla \mathbf{u} \right) = -\nabla p + \nabla \cdot (2\eta \mathbf{D}) + \text{Bo}_m \nabla \cdot \mathbf{\Pi}_M + \mathbf{F}_s + \text{Bo} \rho \mathbf{g}, \quad (17)$$

where the Ohnesorge number  $\text{Oh} = \eta_d / \sqrt{\rho_d \sigma L_c}$ , the magnetic Bond number  $\text{Bo}_m = \mu_0 H_o^2 L_c / \sigma$ , and gravitational Bond number  $\text{Bo} = \rho_d g L_c^2 / \sigma$ .

### 3.3 Spatial discretization

In axisymmetric coordinates  $(r, z, \theta)$ , the magnetic field is given by

$$\mathbf{H} = \left( \frac{\partial \psi}{\partial r}, \frac{\partial \psi}{\partial z}, 0 \right), \quad (18)$$

and the corresponding Maxwell stress is

$$\mathbf{\Pi}_M = \mu \begin{bmatrix} \psi_r^2 - \frac{1}{2}(\psi_r^2 + \psi_z^2) & \psi_r \psi_z & 0 \\ \psi_r \psi_z & \psi_z^2 - \frac{1}{2}(\psi_r^2 + \psi_z^2) & 0 \\ 0 & 0 & -\frac{1}{2}(\psi_r^2 + \psi_z^2) \end{bmatrix}. \quad (19)$$

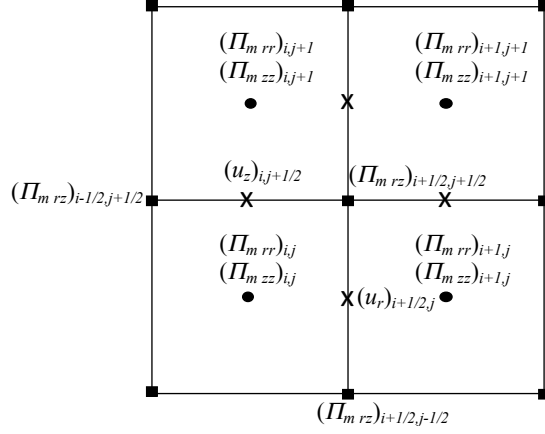


**Fig. 7** Location of the velocities and the magnetic stress tensor components on a MAC grid.

We have

$$\begin{aligned} \nabla \cdot \mathbf{\Pi}_M = & \left[ \frac{1}{r} \frac{\partial}{\partial r} [r(\Pi_M)_{rr}] + \frac{\partial}{\partial z} [(\Pi_M)_{rz}] \right] \mathbf{e}_r \\ & + \left[ \frac{1}{r} \frac{\partial}{\partial r} [r(\Pi_M)_{rz}] + \frac{\partial}{\partial z} [(\Pi_M)_{zz}] \right] \mathbf{e}_z, \end{aligned} \quad (20)$$

where  $\mathbf{e}_r$  and  $\mathbf{e}_z$  are unit vectors in  $r$  and  $z$  directions. The magnetic potential field is discretized using second-order central differences. In axisymmetric coordinates, the discretization of (16) at cell  $(i, j)$  yields, on a regular Cartesian grid of size  $\Delta$ ,

$$\begin{aligned} \nabla \cdot (\mu \nabla \psi)_{i,j} = & \frac{1}{r_{i,j}} \frac{r_{i+1/2,j} \mu_{i+1/2,j} (\frac{\partial \psi}{\partial r})_{i+1/2,j} - r_{i-1/2,j} \mu_{i-1/2,j} (\frac{\partial \psi}{\partial r})_{i-1/2,j}}{\Delta} \\ & + \frac{\mu_{i,j+1/2} (\frac{\partial \psi}{\partial z})_{i,j+1/2} - \mu_{i,j-1/2} (\frac{\partial \psi}{\partial z})_{i,j-1/2}}{\Delta}, \end{aligned} \quad (21)$$

where, for instance for the cell face  $(i+1/2, j)$ ,

$$(\frac{\partial \psi}{\partial r})_{i+1/2,j} = \frac{\psi_{i+1,j} - \psi_{i,j}}{\Delta}. \quad (22)$$

The spatial discretization of the velocity field is based on the MAC grid in figure 7. Therefore, the evaluation of the components of the magnetic stress tensor requires the evaluation of gradients at faces. In axisymmetric coordinates, the divergence of the magnetic stress tensor is discretized in the  $\mathbf{e}_r$  and  $\mathbf{e}_z$  directions

as

$$\begin{aligned} & \frac{1}{r_{i+1/2,j}} \frac{r_{i+1,j}((\Pi_M)_{rr})_{i+1,j} - r_{i,j}((\Pi_M)_{rr})_{i,j}}{\Delta} + \\ & \frac{((\Pi_M)_{rz})_{i+1/2,j+1/2} - ((\Pi_M)_{rz})_{i+1/2,j-1/2}}{\Delta}, \quad \text{and} \\ & \frac{1}{r_{i,j+1/2}} \frac{r_{i+1/2,j+1/2}((\Pi_M)_{rz})_{i+1/2,j+1/2} - r_{i-1/2,j+1/2}((\Pi_M)_{rz})_{i-1/2,j+1/2}}{\Delta} + \\ & \frac{((\Pi_M)_{zz})_{i,j+1} - ((\Pi_M)_{zz})_{i,j}}{\Delta}, \end{aligned} \quad (23)$$

respectively, where, for example, components such as  $((\Pi_M)_{rr})_{i,j}$  and  $((\Pi_M)_{rz})_{i+1/2,j+1/2}$  are discretized as follows

$$\begin{aligned} ((\Pi_M)_{rr})_{i,j} &= \mu_{i,j} \left[ \left( \frac{\psi_{i+1,j} - \psi_{i-1,j}}{2\Delta} \right)^2 \right. \\ & \quad \left. - \frac{1}{2} \left( \left( \frac{\psi_{i+1,j} - \psi_{i-1,j}}{2\Delta} \right)^2 + \left( \frac{\psi_{i,j+1} - \psi_{i,j-1}}{2\Delta} \right)^2 \right) \right], \\ ((\Pi_M)_{rz})_{i+1/2,j+1/2} &= \mu_{i+1/2,j+1/2} \left( \frac{\psi_{i,j} - \psi_{i-1,j} + \psi_{i,j-1} - \psi_{i-1,j-1}}{2\Delta} \right) \times \\ & \quad \left( \frac{\psi_{i-1,j} - \psi_{i-1,j-1} + \psi_{i,j} - \psi_{i,j-1}}{2\Delta} \right) \end{aligned} \quad (24)$$

respectively, where  $\mu_{i+1/2,j+1/2}$  is computed using a simple averaging from cell center values.  $(\Pi_M)_{rr}$  and  $(\Pi_M)_{rz}$  at other grid locations are discretized similarly. Analogous relationships can be written for the other components of the magnetic stress tensor.

### 3.4 Drop deformation under a uniform magnetic field

When a ferrofluid drop is suspended in a non-magnetizable medium in an externally applied uniform magnetic field, it elongates in the direction of the applied magnetic field and assumes a stable equilibrium configuration achieved via the competition between the capillary and magnetic forces. Next, we show the numerical results of the VOF method for a ferrofluid drop suspended in a non-magnetizable viscous medium by Afkhami et al. [2]. The initial configuration for the computational study of a ferrofluid drop suspended in a non-magnetizable viscous medium is shown in figure 8. A uniform magnetic field  $\mathbf{H} = (0, 0, H_o)$ , where  $H_o$  is the magnetic field intensity at infinity, is imposed at the top and bottom boundaries of the computational domain. In order to solve Laplace's equation (16) in the presence of an interface, the following boundary conditions are employed:  $\frac{\partial}{\partial z}\psi = H_o$  at  $z = 0, L_z$ , and  $\frac{\partial}{\partial r}\psi = 0$  at the side boundary  $r = L_r$ . Note that a symmetry condition,  $\frac{\partial}{\partial z}\psi = 0$ , at  $z = 0$ , and  $\frac{\partial}{\partial r}\psi = 0$ , at  $r = 0$  can be applied. The drop radius is  $R_o = 1$  mm, interfacial tension is  $\sigma = 1$  mN m<sup>-1</sup>, and  $\mu_d$  is chosen to be constant.

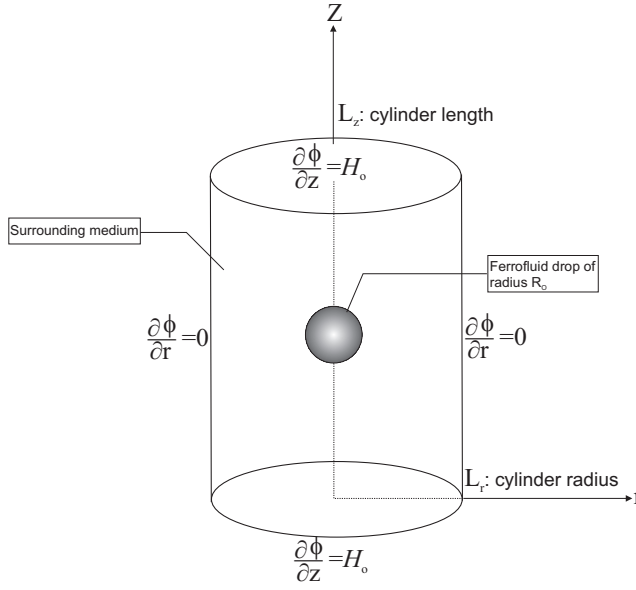


**Fig. 8** Schematic of the initial configuration. The computational domain is  $0 \leq z \leq L_z$ ,  $0 \leq r \leq L_r$ . Initially, a spherical superparamagnetic ferrofluid drop of radius  $R$  is centered in the domain. The boundary conditions on the magnetic field are depicted at the boundaries. Reproduced from [2].

Figure 9(a) shows the results in [2] along with theoretical predictions. The details of the theoretical analysis is given in [2]. From the computational results alone, it is observed that at sufficiently large  $\chi$ , the drop equilibrium aspect ratio jumps to a higher value when the magnetic Bond number reaches a critical value, while for small values of  $\chi$ , the drop equilibrium aspect ratio increases continuously as a function of the magnetic Bond number, in agreement with the theories. Specifically, at  $\chi = 20$ , the jump in drop shape occurs when the magnetic Bond number changes from  $\text{Bo}_m = 0.18$  to  $0.19$ . they also find that for a fixed Figure 9(b) shows the result for  $b/a \approx 7$ ,  $\text{Bo}_m = 0.2$ , and  $\chi = 20$  (see the line -.- in part a), where the shape exhibits conical ends. To provide further insight, the magnetic field lines inside the highly deformed drop as well as in the non-magnetizable surrounding medium, showing the effect of the magnetic field responsible for the appearance of conical ends.

#### 3.4.1 Drop deformation under non-uniform magnetic fields

Here we present the motion of a hydrophobic ferrofluid droplet placed in a viscous medium and driven by an externally applied non-uniform magnetic field is investigated numerically in an axisymmetric geometry. This numerical investigation is motivated by recent developments in the synthesis and characterization of ferrofluids for possible use in the treatment of retinal detachment [22]. Figure 10 shows a cartoon of the application of a small ferrofluid drop injected into the vitreous cavity of the eye and guided by a permanent magnet inserted outside the scleral

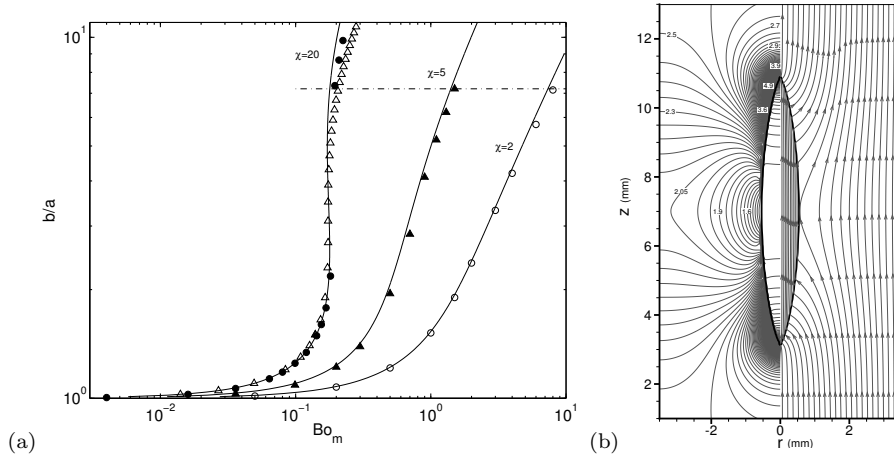


**Fig. 9** From [2]. (a) Comparison of the dependence of the drop aspect ratio  $b/a$  (where  $b$  is the semi-major axis and  $a$  the semi-minor axis) on the magnetic Bond number  $Bo_m$ . Solid lines represent the theoretical analysis in [2]. Numerical results are presented for  $\chi = 2$  ( $\circ$ ),  $\chi = 5$  ( $\blacktriangle$ ) and  $\chi = 20$  ( $\bullet$ ). ( $\triangle$ ) denotes the prediction in [63]. (b) The drop shape and contours of the magnetic field amplitude and magnetic field lines (right) for the highly deformed drop suspended in a non-magnetizable media corresponding to  $b/a \approx 7$ ,  $\chi = 20$ , and  $Bo_m = 0.2$  data point in (a).

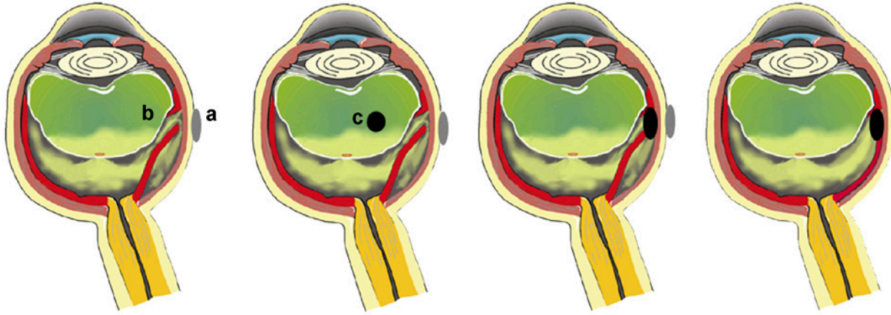


**Fig. 10** Schematic of a procedure for treating the retinal detachment. An external permanent magnet (a), chosen based on its suitability for the given application to the eye surgery, is placed on the eye near the detachment site (b). A ferrofluid droplet (c) is then injected into the eye. The external magnet guides the drop to the site of the tear to seal it. Reproduced from [22].

wall of the eye. The drop travels toward the side of the eye, until it can seal a retinal hole.

To better understand the motion of the ferrofluid droplet moving in the eye, Afkhami et al. [26] present a numerical investigation of a more straightforward scenario where an initially spherical drop is placed at a height  $L$  above the bottom



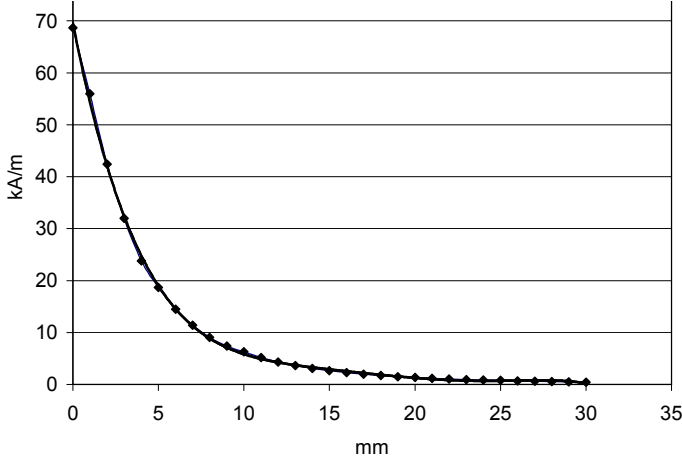


**Fig. 11** From [26]. Measured data for the magnetic field from [22] ( $\blacklozenge$ ) and fifth degree polynomial fitted to the data (—) as functions of the distance from the magnet.

of the cylindrical domain depicted in figure 8. In addition, the boundary condition in the figure is changed to reflect the presence of a magnet at the bottom, which instantly magnetizes the drop. The boundary condition on the magnetic field is reconstructed from the experimental measurements in [22], where the magnitude of  $H(z)$  is measured as a function of distance from the magnet,  $z$ , in the absence of the drop. We then fit the data to a 5th degree polynomial, as shown in figure 11. The scalar potential therefore is a 6th degree polynomial  $\phi(0, z) = P_6(z)$  along the axis of the cylindrical domain. In the absence of the drop,  $\psi$  satisfies Laplace's equation  $\frac{1}{r} \frac{\partial}{\partial r} (r \frac{\partial \psi}{\partial r}) + \frac{\partial^2 \phi}{\partial z^2} = 0$ . If there is a solution, it is analytic and has  $r^2$ -symmetry. The ansatz  $\phi(r, z) = P_6(z) + r^2 P_4(z) + r^4 P_2(z) + r^6 P_0(z)$  yields

$$\phi(r, z) = P_6(z) - \frac{1}{4} r^2 P_6''(z) + \frac{1}{64} r^4 P_6^{(iv)}(z) - \frac{1}{(36)(64)} r^6 P_6^{(vi)}(z). \quad (25)$$

This yields the boundary condition, and also approximates an initial condition when the drop is relatively small. The magnetic potential  $\psi$  is calculated from equation (16). The boundary conditions for  $\psi$  on the domain boundaries  $\partial\Omega$  are defined as

$$\frac{\partial \psi}{\partial n_b} = \frac{\partial \phi}{\partial n_b}, \quad (26)$$

where  $\partial/\partial n_b = \mathbf{n}_b \cdot \nabla$ , and  $\mathbf{n}_b$  denotes the normal to the boundary  $\partial\Omega$ . In order to impose the boundary condition in the numerical model, a transformation of variables is performed to  $\zeta$ :  $\phi = \psi + \zeta$ , where  $\phi$  is the potential field without the magnetic medium. One can then rewrite equation (16) such that

$$\nabla \cdot (\mu \nabla \zeta) = -\nabla \cdot (\mu \nabla \phi), \quad (27)$$

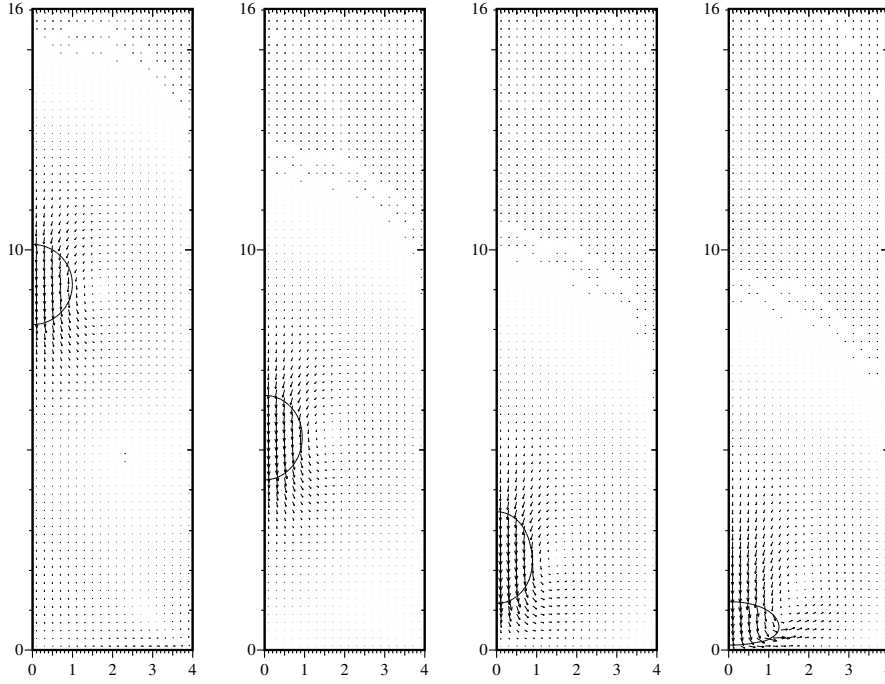


**Fig. 12** Drop shapes along with the velocity fields at times  $t = 120, 160$ , and  $170$  s (from left to right) for a droplet of 2 mm diameter placed 11 mm away from the bottom of the domain, where the magnet is placed. For these simulations,  $Bo_m = 0.06$ . Reproduced from [26].

where  $\nabla \cdot (\mu \nabla \phi)$  vanishes everywhere except on the surface between the drop and the surrounding fluid  $\partial\Omega_f$  and

$$\frac{\partial \zeta}{\partial n} = 0 \text{ on } \partial\Omega. \quad (28)$$

Figure 12 shows direct numerical simulation results for one of the series of experiments conducted in [22]: a droplet of 2 mm diameter placed 11 mm away from the bottom of the domain where the permanent magnet is placed. The figure shows the migration of the drop at times  $t = 120, 160$ , and  $170$  s along with the velocity fields. The travel time compares well with the experimentally measured one in [22]. Additionally, the results show that at an early stage, the flow occurs approximately downwards and only in the region close to the droplet. As the droplet approaches the magnet, it elongates in the vertical direction and vortices induced in the viscous medium become stronger. When the droplet reaches the bottom of the domain, the flow inside the droplet is pumped outward from the center of the droplet, resulting in the flattening of the droplet and consequently a decrease in the droplet height. These observations are consistent with experiments in [22].

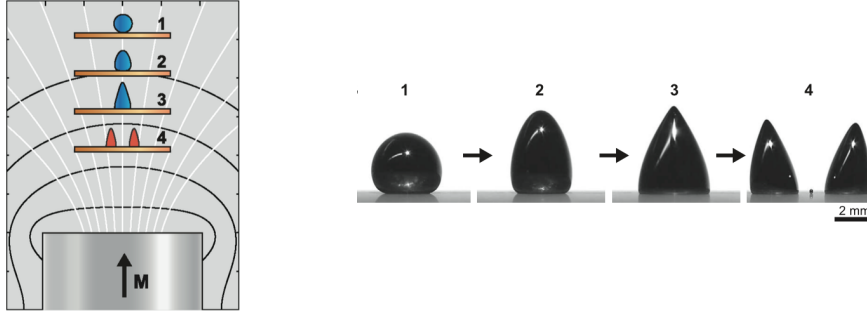


**Fig. 13** Schematic side-view of the experiments from [61]. State of the droplet is: 1, near-zero field; 2, weak field; 3, strong field; and 4, above critical field (drop splits to two daughter droplets). (B) Experimental photographs from [61] of a 20-ml ferrofluid droplet upon increasing the field from 80 Oe (dH/dz 3.5 Oe/mm) to 680 Oe (dH/dz 66 Oe/mm).

### 3.5 Magnetowetting of thin ferrofluid films

Figure 13 shows the phenomenon of magnetowetting for an experiment with magnetic droplets on a superhydrophobic surface, below which is a permanent magnet [61]. By gradually increasing the strength of the magnetic field and the vertical field gradient, the figure shows the transition of the the droplet from a spherical shape into a spiked cone and eventually splitting into two smaller droplets at a critical field strength.

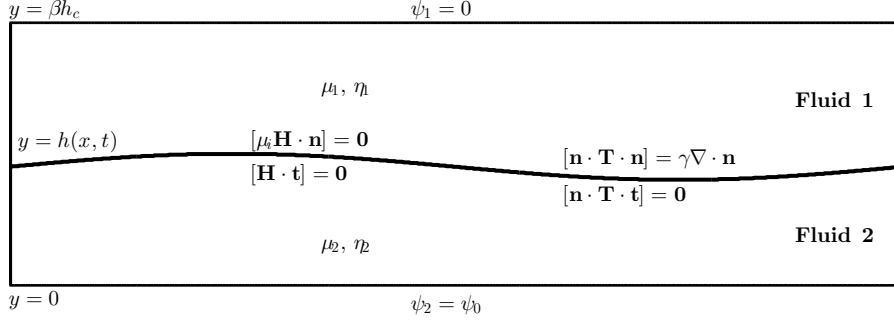
In [39], a problem closely related to magnetowetting is investigated: the application of a uniform magnetic field to induce dewetting of a thin ferrofluid film. Here we present the study in [39], where thin film equations are derived using the long wave approximation of the coupled static Maxwell and Stokes equations and the contact angle is imposed via a disjoining/conjoining pressure model.

Figure 14 shows the schematic of the system of two thin fluid films in the region  $0 < y < \beta h_c$ , with the ferrofluid film occupying the region  $0 < y < h_c$ , and the nonmagnetic fluid occupying the rest of the domain. We denote the permeability and viscosity of the fluids by  $\mu_i$  and  $\eta_i$ , where  $i = (1, 2)$  denotes fluids 1 and 2, respectively. The interface between two fluids is denoted by  $y = h(x, t)$ . The unit normal and tangential vectors to the interface,  $\mathbf{n}$  and  $\mathbf{t}$ , respectively, are given by

$$\mathbf{n} = \frac{1}{(1 + h_x^2)^{1/2}} (-h_x, 1), \quad \mathbf{t} = \frac{1}{(1 + h_x^2)^{1/2}} (1, h_x).$$

Given the small thickness of fluids, we ignore inertial effects and gravity. Hence, the equations governing the motion of the fluids are Stokes equations for continuity and momentum balance,  $\nabla \cdot \mathbf{u} = 0$ ,  $\nabla \cdot \mathbf{T} = 0$ , respectively, where  $\mathbf{T} = -p\mathbf{I} + 2\eta\mathbf{D} + \Pi_M + \Pi_W \mathbf{I}$  is the total stress tensor and the disjoining pressure is specified by

$$\Pi_W(h) = \bar{\kappa} f(h), \quad \text{where } f(h) = (h_*/h)^n - (h_*/h)^m,$$



**Fig. 14** From [39]. The schematic of the system of two thin fluids, where fluid 1 is nonmagnetic and fluid 2 is ferrofluid.

where  $\bar{\kappa} = \sigma \tan^2 \theta / (2Mh_*)$  and  $M = (n - m) / [(m - 1)(n - 1)]$ . In this form,  $II_W$  includes the disjoining/conjoining intermolecular forces due to van der Waals interactions. The prefactor  $\bar{\kappa}$ , that can be related to the Hamaker constant, measures the strength of van der Waals forces. Here,  $h_*$  is the short length scale introduced by the van der Waals potential. We use  $n = 3$  and  $m = 2$ . The contact angle,  $\theta$ , is the angle at which the fluid/fluid interface meets the substrate. The addition of the van der Waals forces is crucial in the present context, since it allows us to study dewetting of thin films under a magnetic field.

We nondimensionalizing the governing equations and boundary conditions using the following scales (dimensionless variables are denoted by tilde)

$$x = x_c \tilde{x}, \quad (y, h) = h_c (\tilde{y}, \tilde{h}), \quad \delta = h_c / x_c, \quad u = u_c \tilde{u}, \quad v = (\delta u_c) \tilde{v},$$

$$p = \left( \eta_2 u_c x_c / h_c^2 \right) \tilde{p}, \quad t = (x_c / u_c) \tilde{t}, \quad \psi = \psi_0 \tilde{\psi},$$

where  $\delta \ll 1$ . The initial thickness of the ferrofluid film is denoted  $h_c$ , and  $u_c$  and  $x_c$  are the characteristic velocity and horizontal length scale, respectively, given by

$$u_c = \frac{\mu_0 \psi_0^2}{\eta_2 x_c}, \quad x_c = \left( \frac{\sigma h_c^3}{\mu_0 \psi_0^2} \right)^{1/2}.$$

Dropping the tilde notation for simplicity, the evolution equation for  $h(x, t)$  then becomes

$$h_t + \frac{1}{3} \frac{1}{x^\alpha} \frac{\partial}{\partial x} \left[ \kappa f'(h) x^\alpha h^3 h_x - \frac{\mu_r (\mu_r - 1)^{-1}}{\left( h - \frac{\beta \mu_r}{\mu_r - 1} \right)^3} h^3 x^\alpha h_x + x^\alpha h^3 \frac{\partial}{\partial x} \left( \frac{1}{x^\alpha} \frac{\partial}{\partial x} (x^\alpha h_x) \right) \right] = 0, \quad (29)$$

where  $\kappa = h_c \sigma \tan^2 \theta / (2\mu_0 \psi_0^2 M h_*)$  is a nondimensional parameter representing the ratio of the van der Waals to the magnetic force,  $\mu_r$  is the ratio of the ferrofluid film permeability to the vacuum permeability,  $\mu_2 / \mu_0$ , and  $\alpha = 0, 1$  for Cartesian and cylindrical coordinates, respectively. The ratio  $\beta \mu_r / (\mu_r - 1)$  is inversely proportional to the magnetic force (note that  $\beta$  is the nondimensional distance between the plates with constant potential, so the gradient of the potential is inversely proportional to  $\beta$ ).

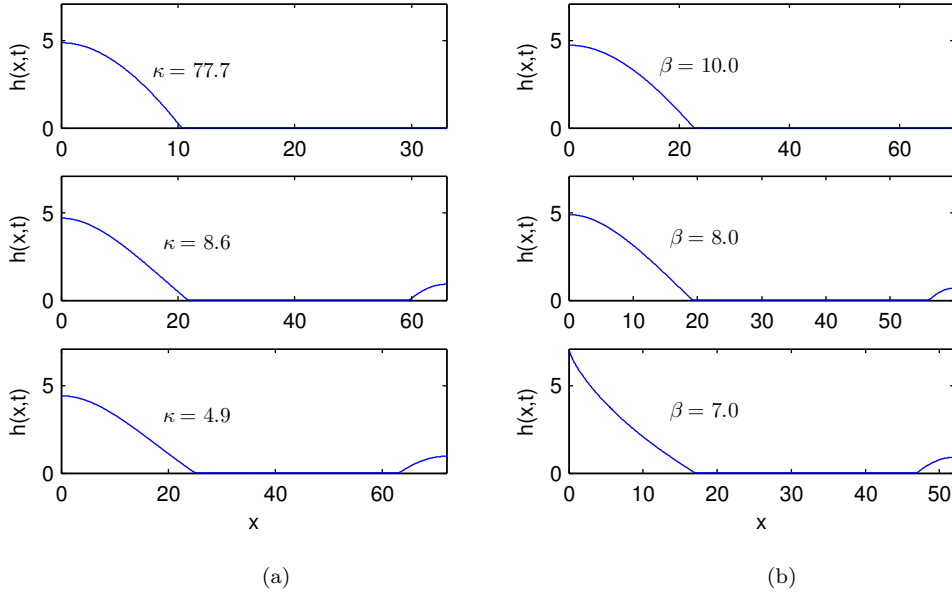


**Fig. 15** From [39]. The effect of varying  $\beta$  and  $\kappa$  on the film evolution when (a)  $\beta = 8$  is fixed, and (b)  $\kappa = 13.5$  is fixed. Note that when  $\beta \leq 7.0$ , no steady-state drop profile can be achieved, indicative of an interfacial instability.

Here we show the thin film simulations of the steady state profiles obtained for a range of parameter values, in particular for nondimensional parameters  $\beta$  and  $\kappa$ . We fix  $\mu_r = 44.6$  and  $h_* = 0.01$ . The initial condition is set to a flat film perturbed around a constant thickness  $h_0$ , i.e.  $h(x, 0) = h_0 + \epsilon \cos(k_m x)$ , with  $\epsilon = 0.1$ , and  $h_0 = 1$ . Here,  $k_m$  is the fastest growing mode computed from the linear stability analysis in [39]. To put this in perspective,  $\kappa = 13.5$ ,  $\beta = 8$ , and  $\mu_r = 44.6$  correspond to values of  $\sigma$  and  $\mu_2$  for an oil-based ferrofluid ( $\sigma = 0.034$  N/m,  $\mu_2 = \mu_0(1 + \chi_m)$ , where  $\chi_m = 3.47 \times 4\pi$ ), and  $\psi_0 = 1.2$  A, and  $\beta$  is chosen to produce a sufficiently strong magnetic field. Making use of the symmetry of the problem, the computational domain is chosen to be equal to one half of the wavelength of the perturbation, i.e.  $L_x = \pi/k_m$ . No flux boundary conditions are imposed at the left and the right end boundaries as  $h' = h''' = 0$ . Figure 15(a) shows the comparison of the steady state profiles for varying parameter  $\kappa$  when keeping  $\beta$  fixed. We note that as  $\kappa$  decreases, i.e. the magnetic force increases compared to the van der Waals force, the satellite droplets start to appear. Similar behavior is observed in figure 15(b) for decreasing values of  $\beta$ ; we observe the formation of satellite droplets for sufficiently small  $\beta$ , i.e. magnetic field dominates over the van der Waals interaction. It should also be noted that the satellite droplets are not present in the simulations where the effect of the magnetic field is ignored (i.e. when  $\mu_r = 1$ ). We also note that for  $\beta = 7.0$  shown in figure 15(b), a static drop cannot be obtained, unlike when  $\beta > 7.0$ : here the height of the fluid approaches the top boundary and the assumptions of the model are not satisfied for the times later than the one at which this profile is shown. The results of simulations suggest that the satellite droplets form when (i) the magnetic force is

sufficiently strong, and (ii) the van der Waals force is sufficiently weak, relative to the magnetic force.

## 4 Conclusion

Biomedical technology is expanding the use of coated superparamagnetic nanoparticles and their suspensions in novel directions; for instance, the delivery of drugs to targeted cells, magnetic resonance imaging, early diagnosis of cancer, treatment such as hyperthermia, and cell separation. The forefront of research lies at the symbiotic development of nanomedicine, nanotechnology, engineering of strong and highly focused magnets, together with numerical algorithms. In this article, three simplified mathematical models have been presented with the aim of producing numerically generated solutions: stochastic differential equations linked to magnetic drug targeting, a volume-of-fluid computational scheme for the motion of a ferrofluid drop through a viscous medium under a magnetic field, and the evolution of a thin film of ferrofluid with numerical investigation of dewetting. An important future direction is the integration of open-source codes for the numerical simulations used with actual biomedical applications. A drawback of commercial software is that the location of numerical inaccuracy in any algorithm is difficult to pinpoint in a black box. The drive toward small scales and complex biomedical domains and materials necessitates a computational approach.

## References

1. X. Liu, M. D. Kaminski, J. S. Riffle, H. Chen, M. Torno, M. R. Finck, L. Taylor, and A. J. Rosengart. Preparation and characterization of biodegradable magnetic carriers by single emulsion-solvent evaporation. *J. Magn. Magn. Mat.*, 311:84–87, 2007.
2. S. Afkhami, A. J. Tyler, Y. Renardy, M. Renardy, R. C. Woodward, T. G. St. Pierre, and J. S. Riffle. Deformation of a hydrophobic ferrofluid droplet suspended in a viscous medium under uniform magnetic fields. *J. Fluid Mech.*, 663:358–384, 2010.
3. S. Balasubramaniam, S. Kayandan, Y. Lin, D. F. Kelly, M. J. House, R. C. Woodward, T. G. St. Pierre, J. S. Riffle, and R. M. Davis. Toward design of magnetic nanoparticle clusters stabilized by biocompatible diblock copolymers for T2-Weighted MRI contrast. *Langmuir*, 30(6):1580–1587, 2014.
4. N. T. Dung, N. V. Long, L. T. T. Tam, P. H. Nam, L. D. Tung, N. X. Phuc, L. T. Lu, and N. T. K. Thanh. High magnetisation, monodisperse and water-dispersible CoFe@Pt core/shell nanoparticles. *Nanoscale*, page 10 pages, 2017.
5. P. A. Voltairas, D.I. Fotiadis, and L.K. Michalis. Hydrodynamics of magnetic drug targeting. *J. Biomechanics*, 35:813–821, 2002.
6. T. Neuberger, B. Schopf, H. Hofmann, M. Hofmann, and B. von Rechenberg. Superparamagnetic nanoparticles for biomedical applications: possibilities and limitations of a new drug delivery system. *J. Magn. Magn. Mater.*, 293 (1):483–496, 2005.
7. C. Buzea, I. I. Pacheco Blandino, and K. Robbie. Nanomaterials and nanoparticles: sources and toxicity. *Biointerphases*, 2 (4):MR17–MR172, 2007.
8. C. C. Berry. Progress in functionalization of magnetic nanoparticles for applications in biomedicine. *J. Phys. D: Appl. Phys.*, 42:224003+9, 2009.
9. B. Mishra, B. B. Patel, and S. Tiwari. Colloidal nanocarriers: a review on formulation technology, types and applications toward targeted drug delivery. *Nanomedicine: Nanotechnology, Biology, and Medicine*, 6:9–24, 2010.
10. A. Nacev, C. Beni, O. Bruno, and B. Shapiro. The behaviors of ferromagnetic nanoparticles in and around blood vessels under applied magnetic fields. *J. Magnetism and Magnetic Materials*, 323:651–668, 2011.

11. A. Ito, M. Shinkai, H. Honda, and T. Kobayashi. Review. medical application of functionalized magnetic nanoparticles. *J. Bioscience and Bioengineering*, 100(1):1–11, 2005.
12. I. K. Puri and R. Ganguly. Particle transport in therapeutic magnetic fields. *Annu. Rev. Fluid Mech.*, 46:407–40, 2014.
13. C. A. Maguire, S. H. Ramirez, S. F. Merkel, M. Sena-Estevés, and X. O. Breakefield. Gene therapy for the nervous system: challenges and new strategies. *Neurotherapeutics*, 11(4):817–839, 2014.
14. K. T. Al-Jamal, J. Bai, J. T. Wang, A. Protti, P. Southern, L. Bogart, H. Heidari, X. Li, A. Cakebread, D. Asker, W. T. Al-Jamal, A. Shah, S. Bals, J. Sosabowski, and Q. A. Pankhurst. Magnetic drug targeting: Preclinical in vivo studies, mathematical modeling, and extrapolation to humans. *Nano Letters*, 16(9):5652–5660, 2016.
15. Leena Mohammed, Hassan G. Gomaa, Doaa Ragab, and Jesse Zhu. Magnetic nanoparticles for environmental and biomedical applications: A review. *Particuology*, 30:1–14, 2017.
16. Patricia Radon, Norbert Loewa, Dirk Gutkelch, and Frank Wiekhorst. Design and characterization of a device to quantify the magnetic drug targeting efficiency of magnetic nanoparticles in a tube flow phantom by magnetic particle spectroscopy. *J. Magn. Magnetic Mat.*, 427:175–180, 2017.
17. Y. K. Suh and S. Kang. Motion of paramagnetic particles in a viscous fluid under a uniform magnetic field: benchmark solutions. *J. Engng Math.*, 69(1):25–58, 2011.
18. Y. Banerjee, P. Bit, R. Ganguly, and S. Hardt. Aggregation dynamics of particles in a microchannel due to an applied magnetic field. *Microfluidics and Nanofluidics*, 13(4):565–577, 2012.
19. A. van Reenen, Y. Gao, A. M. de Jong, M. A. Hulsen, J. M. J. den Toonder, and M. W. J. Prins. Dynamics of magnetic particles near a surface: Model and experiments on field-induced disaggregation. *Phys. Rev. E*, 89(4):042306, 2014.
20. S. S. H. Tsai, I. M. Griffiths, and H. A. Stone. Microfluidic immunomagnetic multi-target sorting – a model for controlling deflection of paramagnetic beads. *Lab on a Chip*, 11:2577–2582, 2011.
21. J. H. Kang, E. Um, A. Diaz, H. Driscoll, M. J. Rodas, K. Domansky, A. L. Watters, M. Super, H. A. Stone, and D. E. Ingber. Optimization of pathogen capture in flowing fluids with magnetic nanoparticles. *Small*, 11(42):5657–5666, 2015.
22. O. T. Mefford, R. C. Woodward, J. D. Goff, T. P. Vadala, T. G. St. Pierre, J. P. Dailey, and J. S. Riffle. Field-induced motion of ferrofluids through immiscible viscous media: Testbed for restorative treatment of retinal detachment. *J. Magn. Magn. Mater.*, 311:347–353, 2007.
23. O. Thompson Mefford, M. R. J. Carroll, M. L. Vadala, J. D. Goff, R. Mejia-Ariza, M. Saunders, R. C. Woodward, T. G. St. Pierre, R. M. Davis, and J. S. Riffle. Size analysis of PDMS-magnetite nanoparticle complexes: Experiment and theory. *Chemistry of Materials*, 20(6):2184–2191, 2008.
24. O. Thompson Mefford, Michael L. Vadala, Matthew R. J. Carroll, Raquel Mejia-Ariza, Beth L. Caba, Timothy G. St. Pierre, Robert C. Woodward, Richey M. Davis, and J. S. Riffle. Stability of Polydimethylsiloxane-magnetite nanoparticles against flocculation: Interparticle interactions of polydisperse materials. *Langmuir*, 24(9):5060–5069, 2008.
25. P. Rowghanian, C. D. Meinhart, and O. Campás. Dynamics of ferrofluid drop deformations under spatially uniform magnetic fields. *J. Fluid Mech.*, 802:245–262, 2016.
26. S. Afkhami, Y. Renardy, M. Renardy, J. S. Riffle, and T. G. St. Pierre. Field-induced motion of ferrofluid droplets through immiscible viscous media. *J. Fluid Mech.*, 610:363–380, 2008.
27. V. Cristini, S. Guido, A. Alfani, J. Blawdziewicz, and M. Loewenberg. Drop breakup and fragment size distribution in shear flow. *J. Rheol.*, 47:1283–1298, 2003.
28. P.J.A. Janssen and P.D. Anderson. A boundary-integral model for drop deformation between two parallel plates with non-unit viscosity ratio drops. *J. Comp. Phys.*, 227:8807–8819, 2008.
29. I. B. Bazhlekova, P. D. Anderson, and H. E. H. Meijer. Numerical investigation of the effect of insoluble surfactants on drop deformation and breakup in simple shear flow. *J. Colloid Interface Sci.*, 298:369–394, 2006.
30. J. Erdmanis, G. Kitenbergs, R. Perzinski, and A. Cēbers. Magnetic micro-droplet in rotating field: numerical simulation and comparison with experiment. *arXiv*, page arXiv:1703.03654v1, 2017.
31. A. V. Lebedev, A. Engel, K. I. Moroznov, and H. Bauke. Ferrofluid drops in rotating magnetic fields. *New Journal of Physics*, 5(57):1–20, 2003.

32. J. J. Feng and C.-Y. Chen. Interfacial dynamics in complex fluids. *J. Fluid Science and Technology*, 11(4), 2016.
33. M. D. Cowley and R. Rosensweig. The interfacial stability of a ferromagnetic fluid. *J. Fluid Mech.*, 30(4):671–688, 1968.
34. R. E. Rosensweig. *Ferrohydrodynamics*. Cambridge University Press New York, 1985.
35. A. Lange, R. Richter, and L. Tobiska. Linear and nonlinear approach to the rosenweig instability. *GAMM-Mitt.*, 30(1):171–184, 2007.
36. H. Kadau, M. Schmitt, M. Wenzel, C. Wink, T. Maier, I. Ferrier-Barbut, and T. Pfau. Observing the rosenweig instability of a quantum ferrofluid. *Nature*, 530:194–197, 2016.
37. O. Lavrova, V. Polevikov, and L. Tobiska. Numerical study of diffusion of interacting particles in a magnetic fluid layer. *Numerical Modeling - InTech*, pages 183–202, 2012.
38. T. G. Kang, Y. Gao, M. A. Hulsen, J. M. J. den Toonder, and P. D. Anderson. Direct simulation of the dynamics of two spherical particles actuated magnetically in a viscous fluid. *Computers and Fluids*, 86:569–581, 2013.
39. I. Seric, S. Afkhami, and L. Kondic. Interfacial instability of thin ferrofluid films under a magnetic field. *JFM Rapids*, 755:755R1, 2014.
40. D. T. Conroy and O. K. Matar. Thin viscous ferrofluid film in a magnetic field. *Phys. Fluids*, 27:092102, 2015.
41. R. V. Craster and O. K. Matar. Electrically induced pattern formation in thin leaky dielectric films. *Phys. Fluids*, 17:032104, 2005.
42. Pengtao Yue, Shernita Lee, Shahriar Afkhami, and Yuriko Renardy. On the motion of superparamagnetic particles in magnetic drug targeting. *Acta Mechanica*, 223(3):505–527, 2012.
43. LifeForce Hospitals Webserver medmail@usa.net. <http://chemo.net/newpage91.htm>, Copyright 1999.
44. S. D. House and P. C. Johnson. Diameter and blood flow of skeletal muscle venules during local flow regularization. *Am. J. Physiol. Heart Circ. Physiol.*, 250:H828–H837, 1986.
45. E. G. D. Cohen and R. van Zon. Stationary state fluctuation theorems for driven Langevin systems. *Comptes Rendus Physique*, 8:507–517, 2007.
46. D. J. Higham. An algorithmic introduction to numerical simulation of stochastic differential equations. *SIAM Review*, 43:525–546, 2001.
47. Umberto Picchini. SDE Toolbox: simulation and estimation of stochastic differential equations with Matlab. <http://sdetoolbox.sourceforge.net/>, 2009.
48. L. C. Barnsley, D. Carugo, M. Aron, and E. Stride. Understanding the dynamics of superparamagnetic particles under the influence of high field gradient arrays. *Phy. Med. Biol.*, 62:2333–2360, 2017.
49. L. Sprenger, S. Dutz, T. Schneider, S. Odenbach, and U. O. Haefeli. Simulations and experimental determination of the online separation of blood components with the help of microfluidic cascading spirals. *Biomicrofluidics*, 9, 2015.
50. E. M. Cherry and J. K. Eaton. A comprehensive model of magnetic particle motion during magnetic drug targeting. *Int. J. Mult. Flow*, 59:173–185, 2014.
51. I. Rukshin, J. Mohrenweiser, P. Yue, and S. Afkhami. Modeling superparamagnetic particles in blood flow for applications in magnetic drug targeting. *Fluids*, submitted:(13 pages), 2017.
52. I. M. Griffiths and H. A. Stone. Axial dispersion via shear-enhanced diffusion in colloidal suspensions. *Europhysics Letters*, 97(5):58001–p1 – p6, 2012.
53. O. Lavrova, G. Matthies, T. Mitkova, V. Polevikov, and L. Tobiska. Numerical treatment of free surface problems in ferrohydrodynamics. *J. Phys.: Condens. Matter*, 18(38):S2657–S2669, 2006.
54. O. Lavrova, G. Matthies, V. Polevikov, and L. Tobiska. Numerical modeling of the equilibrium shapes of a ferrofluid drop in an external magnetic field. *Proc. Appl. Math. Mech.*, 4:704–705, 2004.
55. V. Bashtovoi, O. A. Lavrova, V. K. Polevikov, and L. Tobiska. Computer modeling of the instability of a horizontal magnetic-fluid layer in a uniform magnetic field. *J. Magn. Magn. Mater.*, 252:299–301, 2002.
56. G. Matthies and L. Tobiska. Numerical simulation of normal-field instability in the static and dynamic case. *J. Magn. Magn. Mater.*, 289:346–349, 2005.
57. H. Knieling, R. Richter, I. Rehberg, G. Matthies, and A. Lange. Growth of surface undulations at the Rosensweig instability. *Phys. Rev. E*, 76:066301, 2007.
58. R. Scardovelli and S. Zaleski. Direct numerical simulation of free surface and interfacial flow. *Ann. Rev. Fluid Mech.*, 31:567–604, 1999.



- 
59. P. Smereka J. Sethian. Level-set methods for fluid interfaces. *Ann. Rev. Fluid. Mech.*, 35:341–372, 2003.
  60. D. M. Anderson, G. B. McFadden, and A. A. Wheeler. Diffuse-interface methods in fluid mechanics. *Ann. Rev. Fluid Mech.*, 30:139–166, 1998.
  61. J.V.I. Timonen, M. Latikka, L. Leibler, R.H.A. Ras, and O. Ikkala. Switchable static and dynamic self-assembly of magnetic droplets on superhydrophobic surfaces. *Science*, 341:253, 2013.
  62. J. U. Brackbill, D. B. Kothe, and C. Zemach. A continuum method for modeling surface tension. *J. Comput. Phys.*, 100:335–354, 1992.
  63. J. C. Bacri and D. Salin. Instability of ferrofluid magnetic drops under magnetic field. *J. Phys. Lett.*, 43:649–654, 1982.